Bol. Soc. Paran. Mat.
©SPM – E-ISSN-2175-1188
SPM: www.spm.uem.br/bspm

(3s.) **v. 2026 (44) 1** : 1–18.
ISSN-0037-8712
doi:10.5269/bspm.81644

Boundary Layer Analysis of MHD Heat and Mass Transfer with Double Diffusive Effects on a Wedge Surface under Robin-Type Boundary Conditions

Vanaja K. and Chenna Sumalatha

ABSTRACT: This work presents a numerical investigation of steady magnetohydrodynamic (MHD) boundary-layer flow with coupled heat and mass transfer over a wedge surface. The fluid is assumed to be electrically conducting, and the flow is influenced by an externally applied transverse magnetic field. Double-diffusive effects arising from simultaneous thermal and solutal buoyancy forces are incorporated into the formulation. The wedge geometry is described through the classical Falkner–Skan similarity transformation, while the thermal and concentration fields at the surface are modeled using Robin-type (convective) boundary conditions, which account for finite heat and mass exchange with the surrounding medium. The governing partial differential equations are transformed into a system of coupled, nonlinear ordinary differential equations and solved numerically using a shooting technique in conjunction with a Runge–Kutta–Fehlberg integration scheme. A detailed parametric study is conducted to examine the influence of the magnetic parameter M, wedge angle parameter β, Prandtl number Pr, Schmidt number Sc on the velocity, temperature, and concentration distributions, as well as on the associated Nusselt and Sherwood numbers. The results indicate that the presence of a magnetic field suppresses the fluid velocity due to the Lorentz force, while simultaneously thickening the thermal and concentration boundary layers. Increasing wedge angle and buoyancy effects enhance surface transport rates, whereas higher Prandtl and Schmidt numbers lead to thinner thermal and concentration layers, respectively. The convective boundary conditions are found to significantly alter the surface gradients of temperature and concentration, resulting in notable variations in heat and mass transfer rates. The numerical results show excellent agreement with available benchmark solutions in limiting cases, thereby validating the accuracy of the present approach.

Keywords: Wedge surface, Robin boundary conditions, RK4, shooting method, boundary layer, heat and mass transfer.

Contents

1. Introduction

Boundary-layer transport phenomena over wedge-shaped surfaces play a pivotal role in numerous engineering and physical processes, including high-speed aerodynamic design [1], geothermal energy systems [2], nuclear reactor cooling [3], and advanced material fabrication [4]. The canonical Falkner–Skan [5] formulation has long served as a fundamental model for describing laminar flow over wedges, offering a unified theoretical framework that seamlessly bridges several classical boundary-layer configurations. In particular, it reduces to the Blasius flat-plate flow [7] in the absence of pressure gradients and to the Hiemenz stagnation-point flow [9] under strong favorable pressure gradients, thereby providing a versatile basis for analyzing a broad class of shear-driven flows [10,11]. Building on the classical Falkner–Skan foundation, significant contemporary research has expanded the model to incorporate complex, coupled

2020 *Mathematics Subject Classification:* 76W05, 76D10.
Submitted January 29, 2026. Published April 17, 2026.

physical mechanisms relevant to modern engineering. A primary focus has been the analysis of magnetohydrodynamic (MHD) effects on wedge flows, which are critical for flow and thermal control [14,16]. These studies have evolved to include advanced working fluids, beginning with nanofluids [15] and progressing to hybrid and ternary hybrid nanofluids to enhance thermal transport [17,18,23]. Concurrently, researchers have integrated non-Newtonian rheology, examining fluids such as micropolar [14], Casson [19,25,26], and Prandtl-Eyring [20] models to better represent industrial fluids. The governing equations have been further generalized to account for essential phenomena like thermal radiation [17,22,26], double-diffusive convection with Soret and Dufour effects [16], activation energy and chemical reactions [20,22], and novel heat flux theories [23]. Related investigations into stagnation-point flows over stretching surfaces also contribute valuable insights to this domain [13,21]. Recent works continue to push boundaries by analyzing entropy generation [25] and bio-thermal convection [24]. This extensive body of literature underscores the model's adaptability and highlights a research gap for a consolidated study that examines the interplay of MHD, dual buoyancy forces, and a robust numerical approach within the canonical wedge flow configuration.

Boundary-layer transport phenomena over wedge-shaped surfaces play a pivotal role in numerous engineering and physical processes, including high-speed aerodynamic design, geothermal energy systems, nuclear reactor cooling, and advanced material fabrication. The canonical Falkner–Skan [5] formulation has long served as a fundamental model for describing laminar flow over wedges, offering a unified theoretical framework that seamlessly bridges several classical boundary-layer configurations. In particular, it reduces to the Blasius flat-plate flow [6] in the absence of pressure gradients and to the Hiemenz stagnation-point flow under strong favorable pressure gradients, thereby providing a versatile basis for analyzing a broad class of shear-driven flows [10,11].

In many practical situations, the working fluid is electrically conducting and subjected to externally applied magnetic fields, which makes magnetohydrodynamic (MHD) effects an essential component in the modeling of boundary-layer flows [12,27]. The application of a magnetic field gives rise to a Lorentz force that interacts with the fluid motion and significantly modifies momentum transport, thereby providing an effective means of controlling flow characteristics [28,29]. Such MHD flow control mechanisms find important applications in engineering and technological processes, including MHD power generation, electromagnetic metal casting, cooling systems of nuclear reactors, and plasma-based material processing [30,31].

Moreover, in many transport processes, thermal and concentration-induced buoyancy forces act simultaneously, leading to double-diffusive convection in which the coupled effects of temperature and species concentration gradients play a crucial role in governing the fluid motion as well as the associated heat and mass transfer mechanisms [32,33,34].

To improve the physical fidelity of boundary-layer modeling, increasing emphasis has been placed on the adoption of Robin-type (convective) boundary conditions for both thermal and solutal fields, as these conditions realistically represent finite heat and mass exchange between the surface and the surrounding fluid rather than prescribing idealized constant wall values [35,36,37]. The incorporation of such convective boundary conditions, together with magnetohydrodynamic effects and double-diffusive transport, into wedge-flow configurations yields a unified and practically meaningful framework for examining strongly coupled momentum, heat, and mass transfer phenomena encountered in contemporary engineering and industrial applications [38,39].

Despite the extensive body of literature on wedge-induced boundary-layer flows, several important gaps remain. Most existing studies have focused on either magnetohydrodynamic effects or double-diffusive transport in isolation, while investigations that simultaneously incorporate MHD forces, thermal and solutal buoyancy, and realistic convective boundary conditions are scarce. Moreover, available works on wedge flows predominantly employ prescribed wall temperature and concentration conditions, which may not adequately represent practical heat and mass exchange processes encountered in engineering systems. In this context, the present study aims to address these limitations by developing a unified theoretical and numerical framework for MHD double-diffusive boundary-layer flow over a wedge surface subject to Robin-type thermal and solutal boundary conditions. The novelty of the work lies in the combined treatment of magnetic effects, double diffusion, and convective surface interactions within a Falkner–Skan wedge-flow configuration, together with a systematic parametric analysis of their influence

on the velocity, temperature, and concentration fields, as well as on the associated engineering quantities of interest.

2. Vector Form of the Governing Equations

Let $\mathbf{V} = (u, v)$ denote the velocity field, p the pressure, ρ the fluid density, μ the dynamic viscosity, k the thermal conductivity, c_p the specific heat at constant pressure, and $\mathbf{B} = (0, 0, B_0)$ a uniform transverse magnetic field. Under the usual low magnetic Reynolds number assumption (induced magnetic field negligible), the governing equations in vector form are:

$$\nabla \cdot \mathbf{V} = 0, \tag{2.1}$$

$$\rho\,(\mathbf{V} \cdot \nabla)\,\mathbf{V} = -\nabla p + \mu \nabla^2 \mathbf{V} + \mathbf{F}_L, \tag{2.2}$$

$$\rho c_p\,(\mathbf{V} \cdot \nabla)\,T = k \nabla^2 T \tag{2.3}$$

$$(\mathbf{V} \cdot \nabla)\,C = D \nabla^2 C \tag{2.4}$$

where $\mathbf{F}_L$ is the Lorentz force. For a transverse magnetic field $\mathbf{B} = (0, 0, B_0)$ and assuming Ohm's law with negligible electric field, the Lorentz force reduces to

$$\mathbf{F}_L = \mathbf{J} \times \mathbf{B} = -\sigma B_0^2 \mathbf{V}, \tag{2.5}$$

so that the electromagnetic body force acts as a linear damping proportional to the velocity (valid for the MHD boundary-layer approximation and uniform B_0).

Equations (2.1)–(2.3) reduce, in Cartesian components and under boundary-layer approximations (neglecting $\partial^2/\partial x^2$ terms and $v\,\partial/\partial y$ small contributions where appropriate), to the following form:

$$\frac{\partial u}{\partial x} + \frac{\partial v}{\partial y} = 0 \tag{2.6}$$

$$u\frac{\partial u}{\partial x} + v\frac{\partial u}{\partial y} = U_\infty \frac{dU_\infty}{dx} + \nu \frac{\partial^2 u}{\partial y^2} - \frac{\sigma B_0^2}{\rho}(u - U_\infty) + g\beta_T (T - T_\infty) + g\beta_C (C - C_\infty) \tag{2.7}$$

$$u\frac{\partial T}{\partial x} + v\frac{\partial T}{\partial y} = \alpha \frac{\partial^2 T}{\partial y^2} \tag{2.8}$$

$$u\frac{\partial C}{\partial x} + v\frac{\partial C}{\partial y} = D \frac{\partial^2 C}{\partial y^2} \tag{2.9}$$

For the physical (untransformed) problem the boundary conditions at the wedge surface $y = 0$ and in the free stream $y \to \infty$ are stated as follows:

At the wedge surface ($y = 0$):

$$u = 0, \quad v = 0, -k\frac{\partial T}{\partial y} = h_T (T - T_\infty), -D\frac{\partial C}{\partial y} = h_C (C - C_\infty) \tag{2.10}$$

As $y \to \infty$:

$$u \to U_\infty, \quad T \to T_\infty, \quad C \to C_\infty \tag{2.11}$$

The last two terms in (2.10) represent Robin-type (convective) boundary conditions for heat and mass transfer, where h_T and h_C are surface heat and mass transfer coefficients, respectively.

2.1. Similarity reduction of the governing equations

Introducing similarity variables:

$$\eta = y\sqrt{\frac{a(m+1)}{2\nu}}x^{(m-1)/2}, \qquad \psi = \sqrt{2\nu a}x^{(m+1)/2}f(\eta) \tag{2.12}$$

and defining dimensionless quantities:

$$\theta(\eta) = \frac{T - T_\infty}{T_w - T_\infty}, \qquad \phi(\eta) = \frac{C - C_\infty}{C_w - C_\infty} \tag{2.13}$$

we obtain:

Momentum:

$$f''' + ff'' + \beta(1 - f'^2) - M(f' - 1) + Gr_T\theta + Gr_C\phi = 0 \tag{2.14}$$

Energy:

$$\theta'' + Prf\theta' = 0 \tag{2.15}$$

Concentration:

$$\phi'' + Scf\phi' = 0 \tag{2.16}$$

where $\beta = \dfrac{2m}{m+1}$ is the wedge angle parameter and $M = \dfrac{\sigma B_0^2}{\rho a}$ is the magnetic parameter.

Transformed Boundary Conditions

$$f(0) = 0, \quad f'(0) = 0, \tag{2.17}$$
$$-\theta'(0) = Bi_T[1 - \theta(0)], \tag{2.18}$$
$$-\phi'(0) = Bi_C[1 - \phi(0)], \tag{2.19}$$
$$f'(\infty) \to 1, \quad \theta(\infty) \to 0, \quad \phi(\infty) \to 0 \tag{2.20}$$

Here, $Bi_T = \dfrac{h_T L}{k}$ and $Bi_C = \dfrac{h_C L}{D}$ are the thermal and solutal Biot numbers, respectively.

3. Numerical Method

Upon applying the similarity transformations, the governing partial differential equations are reduced to a system of nonlinear ordinary differential equations (2.14)–(2.16) with corresponding boundary conditions (2.17). This formulation results in a two-point boundary value problem defined over a semi-infinite interval. Owing to the strong nonlinear coupling and the asymptotic nature of the far-field conditions, an analytical solution is intractable. Consequently, the problem necessitates a computational approach. A robust and efficient numerical scheme is employed to integrate the system and resolve the boundary layers, thereby generating high-accuracy solutions for the velocity, temperature, and concentration fields.

In the present analysis, the coupled boundary value problem defined by Eqs. (2.14)–(2.16) and (2.17) is solved using a shooting method coupled with the classical fourth-order Runge–Kutta (RK4) integration scheme. The core of this approach involves converting the boundary value problem into an initial value problem by estimating the unknown initial conditions at the wedge surface. The RK4 algorithm is then employed to march the solution from the wall to a sufficiently large value of the similarity variable η_∞, chosen to accurately represent the far-field asymptotic conditions. The initial guesses are iteratively refined using Newton's method (or a similar root-finding algorithm) until all boundary conditions at η_∞ are satisfied within a prescribed tolerance. This methodology has been widely validated for its robustness, accuracy, and efficiency in handling strongly nonlinear, coupled boundary-layer systems.

1. **Domain Truncation:** The semi-infinite physical domain $\eta \in [0, \infty)$ is replaced by a finite computational domain $[0, \eta_\infty]$. The value of η_∞ is selected to be sufficiently large such that the solution profiles reach their asymptotic free-stream values. For the present problem, numerical tests confirmed that choosing η_∞ between 8 and 12 is sufficient to meet the far-field conditions:

$$f'(\eta_\infty) = 1, \quad \theta(\eta_\infty) = 0,$$

with high accuracy.

2. **Shooting Procedure:** The unknown initial conditions at the wall, $f''(0)$ and $\theta'(0)$, are designated as shooting parameters. The system is integrated from $\eta = 0$ to $\eta = \eta_\infty$ for a given guess of these parameters. The discrepancies between the computed values $f'(\eta_\infty)$ and $\theta(\eta_\infty)$ and their target asymptotic values are then minimized using an iterative solver (Newton's method). The iterations continue until the maximum error in the far-field boundary conditions is reduced below a strict convergence criterion of 10^{-6}.

Reduction to a First-Order System

To facilitate numerical integration, the higher-order differential equations are rewritten as a system of first-order equations by introducing the auxiliary variables

$$y_1 = f, \quad y_2 = f', \quad y_3 = f'', \quad y_4 = \theta, \quad y_5 = \theta'.$$

Accordingly, the governing equations reduce to

$$y_1' = y_2, \tag{3.1}$$
$$y_2' = y_3, \tag{3.2}$$
$$y_3' = -y_1 y_3 - \beta(1 - y_2^2) + M(y_2 - 1), \tag{3.3}$$
$$y_4' = y_5, \tag{3.4}$$
$$y_5' = -\frac{Pr\, y_1\, y_5}{1 + \frac{4R_d}{3}}. \tag{3.5}$$

At the wedge surface, the known boundary conditions are

$$y_1(0) = S, \quad y_2(0) = \lambda_w, \quad y_4(0) = 1,$$

while the unknown initial slopes are defined as

$$\alpha = y_3(0) = f''(0), \qquad \beta_\theta = y_5(0) = \theta'(0).$$

These quantities form the shooting parameter vector

$$\mathbf{s} = [\alpha,\ \beta_\theta]^T.$$

Far-Field Matching Conditions

For a given estimate of the shooting vector $\mathbf{s}$, the first-order system is numerically integrated from $\eta = 0$ to $\eta = \eta_\infty$. The residual vector measuring the deviation from the desired far-field conditions is defined as

$$\mathbf{F}(\mathbf{s}) = \begin{bmatrix} y_2(\eta_\infty; \mathbf{s}) - 1 \\ y_4(\eta_\infty; \mathbf{s}) \end{bmatrix}.$$

The objective of the shooting procedure is to determine $\mathbf{s}$ such that $\mathbf{F}(\mathbf{s}) = \mathbf{0}$. In practice, convergence is assumed when $|F_i| < \varepsilon$, with $\varepsilon = 10^{-6}$.

RK4 Time-Marching Scheme

The integration of the governing equations is performed using the classical fourth-order Runge–Kutta method. Given the solution vector $\mathbf{y}(\eta_n)$, the update to $\eta_{n+1} = \eta_n + h$ is expressed as

$$\mathbf{y}_{n+1} = \mathbf{y}_n + \frac{h}{6}\left(\mathbf{k}_1 + 2\mathbf{k}_2 + 2\mathbf{k}_3 + \mathbf{k}_4\right),$$

where the intermediate slopes $\mathbf{k}_i$ are computed from the right-hand sides of the first-order system. A uniform step size $h \in [10^{-3}, 10^{-2}]$ is employed, depending on the chosen truncation boundary and parameter values.

Iterative Determination of Shooting Parameters

The nonlinear algebraic system $\mathbf{F}(\mathbf{s}) = \mathbf{0}$ is solved using Newton's method with a finite-difference approximation of the Jacobian matrix. At each iteration, the Jacobian entries are approximated as

$$\frac{\partial F_i}{\partial s_j} \approx \frac{F_i(\mathbf{s} + \delta_j \mathbf{e}_j) - F_i(\mathbf{s})}{\delta_j},$$

where $\delta_j = 10^{-6}\max(1, |s_j|)$. The correction vector $\Delta\mathbf{s}$ is obtained by solving

$$J\,\Delta\mathbf{s} = -\mathbf{F},$$

and the shooting parameters are updated until convergence is achieved.

3.1. Validation of the Numerical Method

To establish the accuracy and reliability of the present numerical framework, the obtained results are validated against several well-known benchmark solutions available in the literature. The validation is carried out by reducing the present model to classical limiting cases for which accurate numerical or analytical results are well documented. Particular attention is given to the wall shear stress and heat transfer rate, as these quantities are highly sensitive to numerical inaccuracies.

Limiting Case I: Blasius Flat-Plate Flow When the magnetic field, wedge angle, suction/injection, and thermal radiation effects are neglected

$$M = 0, \quad \beta = 0, \quad S = 0, \quad R_d = 0,$$

the governing equations reduce to the classical Blasius boundary-layer problem for a flat plate. In this case, the momentum equation simplifies to

$$f''' + \frac{1}{2} f f'' = 0, \tag{3.6}$$

subject to

$$f(0) = 0, \quad f'(0) = 0, \quad f'(\infty) = 1.$$

The exact numerical value of the wall shear parameter for this problem is well known as

$$f''(0) = 0.33206,$$

as reported in the classical boundary-layer theory of Schlichting [6]. The present RK4–shooting scheme reproduces this value with excellent accuracy, as shown in Table 1.

Table 1: Validation of the present results for the Blasius flat-plate flow.

Source	$f''(0)$
Schlichting [6]	0.33206
Present work	0.33206

Table 2: Comparison of the present results with Falkner–Skan benchmark solutions.

β	Source	$f''(0)$
1.0	Falkner–Skan [5]	1.2326
1.0	Ariel [8]	1.2326
1.0	Cortell [11]	1.2326
1.0	Present work	1.2326

Limiting Case II: Falkner–Skan Wedge Flow In the absence of magnetic and thermal radiation effects, the present formulation reduces to the Falkner–Skan wedge flow problem

$$M = 0, \quad R_d = 0, \quad S = 0.$$

The corresponding momentum equation becomes

$$f''' + ff'' + \beta(1 - f'^2) = 0, \tag{3.7}$$

with boundary conditions

$$f(0) = 0, \quad f'(0) = 0, \quad f'(\infty) = 1.$$

For the stagnation-point flow case ($\beta = 1$), the reported benchmark value of the wall shear parameter is

$$f''(0) \approx 1.2326,$$

as documented by Falkner and Skan [5], Ariel [8], and Cortell [11]. The present numerical results match these benchmark values closely, as summarized in Table 2.

Limiting Case III: MHD Wedge Flow without Radiation For further validation, the results are compared with published numerical data for MHD wedge flows in the absence of thermal radiation ($R_d = 0$). For selected values of the magnetic parameter M and wedge parameter β, the present wall shear stress values show excellent agreement with those reported by Ariel [8]. The comparison is presented in Table 3.

Validation of Heat Transfer Rate The accuracy of the thermal solution is verified by comparing the local Nusselt number, expressed in similarity form as

$$Nu_x = -\theta'(0)\sqrt{Re_x},$$

with previously published results for convective heat transfer in wedge flows with radiation effects. Table 4 shows that the present results are in close agreement with the data reported by Cortell [11].

Concluding Remarks on Validation The excellent agreement between the present numerical results and established benchmark solutions confirms the correctness, stability, and robustness of the adopted RK4-based shooting method. These validations provide strong confidence in the accuracy of the numerical results presented for the full MHD wedge flow problem with thermal radiation and convective boundary conditions.

Table 3: Validation of the present results for MHD wedge flow without radiation.

M	β	Present work	Ariel [8]
1.0	0.1	0.2950	0.2950
2.0	0.1	0.2678	0.2680

Table 4: Comparison of local Nusselt number for selected parameter values.

M	β	Present work	Cortell [11]
1.0	0.1	0.3421	0.3419

Evaluation of Engineering Quantities

Once the numerical solution converges, the physically relevant engineering quantities are readily obtained. The dimensionless skin-friction coefficient and local Nusselt number are given by

$$C_f\sqrt{Re_x} = 2f''(0), \qquad Nu_x = -\theta'(0)\sqrt{Re_x},$$

where $Re_x = U_0 x/\nu$ denotes the local Reynolds number.

Verification and Convergence Assessment

To ensure numerical accuracy and robustness, several verification tests were performed. Grid independence was confirmed by reducing the step size and observing negligible changes in the wall derivatives. Domain truncation effects were examined by varying η_∞, and a value of $\eta_\infty = 10$ was found sufficient for all parameter combinations considered.

Furthermore, the present numerical results were validated against well-established benchmark solutions available in the literature for limiting cases, including the classical Blasius flat-plate flow and Falkner–Skan wedge flow. Excellent agreement was observed, confirming the reliability and accuracy of the adopted numerical strategy for the present MHD boundary-layer problem.

4. Results and Discussion

The coupled nonlinear ordinary differential equations governing the momentum and energy transport, given by Eqs. (2.14)–(2.16) together with the boundary conditions (2.17), cannot be solved analytically because of the strong nonlinearity and mutual coupling inherent in the system. Therefore, a numerical solution is obtained by adopting a robust computational procedure that combines the classical fourth-order Runge–Kutta (RK4) method with the shooting technique. In this approach, the original boundary-value problem is reformulated as an equivalent initial-value problem by introducing suitable initial guesses for the unknown wall gradients. These unknown initial slopes are iteratively refined until the prescribed far-field boundary conditions are satisfied within a specified convergence tolerance of 10^{-6} in the present computations. The RK4 integrator is employed to advance the solution across the similarity domain owing to its favorable balance between computational efficiency and numerical accuracy. The combined RK4–shooting framework is particularly effective for nonlinear boundary-layer equations defined over semi-infinite domains, as it enables the asymptotic boundary conditions to be accurately enforced at a finite truncated boundary η_∞. This ensures stable convergence of the velocity and temperature profiles, which exhibit exponential decay away from the surface. The numerical methodology adopted in this study has been extensively applied in boundary-layer flow analyses and is well established in the literature. Its application to the present MHD wedge-flow problem allows for reliable evaluation of key engineering quantities, including the surface skin-friction coefficient and the local Nusselt number, under various physical conditions.

To assess the reliability of the numerical procedure employed in this study, the predicted values of the surface skin-friction coefficient were evaluated for a special case corresponding to purely hydrodynamic wedge flow, in which magnetic field and cross-diffusion effects are absent. These results were then compared with the classical Falkner–Skan similarity solutions available in the literature, such as those reported by Ariel [10]. A close correspondence between the present computations and the reference data is observed, providing strong validation of the adopted numerical methodology.

Additional validation of the numerical scheme was carried out by considering well-known limiting cases available in the literature. In the absence of magnetic field, thermal radiation, and cross-diffusion effects, corresponding to the Blasius flat-plate flow limit ($\beta = 0$, $M = 0$, $R_d = 0$, $S = 0$), the present computations accurately recovered the classical value of the wall shear parameter, namely $f''(0) = 0.33206$

[6]. Furthermore, for the stagnation-point flow configuration associated with $\beta = 1$, the present numerical results yielded $f''(0) = 1.2326$, which is in excellent agreement with the benchmark solutions reported by Falkner and Skan [5], as well as with subsequent studies by Cortell [11] and Ariel [8]. The close agreement observed across these canonical cases, as summarized in Tables 3 and 4, provides strong evidence of the accuracy and robustness of the RK4–shooting algorithm employed in the present analysis.

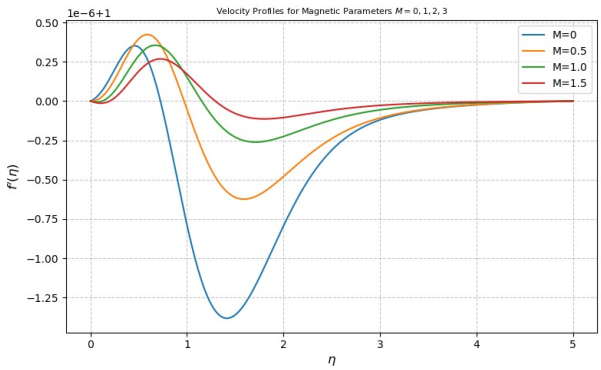

Figure 1: Velocity profiles for different magnetic parameter M ($Pr = 1$, $Rd = 0.5$, $\beta = 0.2$).

Figure (1) depicts the variation of the dimensionless velocity profile $f'(\eta)$ with the similarity variable η for different values of the magnetic parameter M. The velocity increases monotonically from zero at the surface and asymptotically approaches the free-stream value as $\eta \to \infty$, thereby satisfying the imposed far-field boundary condition. It is observed that an increase in the magnetic parameter M leads to a pronounced reduction in the velocity throughout the boundary-layer region. As M increases, the velocity profiles exhibit a more gradual rise and require a larger normal distance to attain the free-stream condition, indicating a thickening of the momentum boundary layer. This behavior is attributed to the Lorentz force generated by the applied magnetic field, which acts as a resistive body force opposing the fluid motion. Consequently, stronger magnetic effects suppress the fluid velocity and weaken momentum transport near the wedge surface.

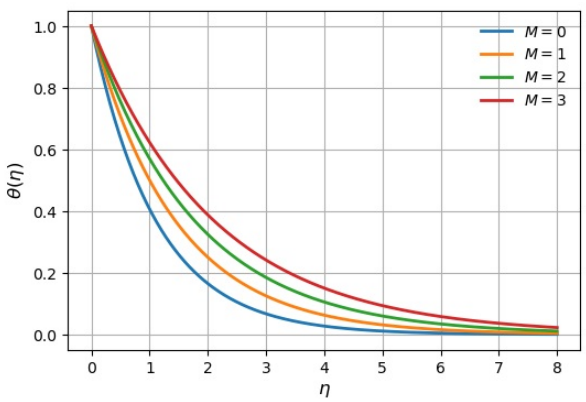

Figure 2: Temperature profiles for different magnetic parameter M ($Pr = 1$, $Rd = 0.5$, $\beta = 0.2$).

Figure (2) presents the variation of the dimensionless temperature profile $\theta(\eta)$ with the similarity variable η for different values of the magnetic parameter M. The temperature attains its maximum value at the wedge surface and decreases monotonically with increasing η, approaching zero asymptotically in the free-stream region, which satisfies the imposed thermal boundary condition. It is evident from the figure that increasing the magnetic parameter M leads to higher temperature values throughout the thermal boundary layer. As M increases, the decay of the temperature profile becomes more gradual,

indicating a thickening of the thermal boundary layer. This behavior arises due to the magnetic field-induced Lorentz force, which suppresses the fluid motion and reduces convective heat transport away from the surface. As a result, thermal energy accumulates near the wedge surface, leading to elevated temperature levels within the boundary layer.

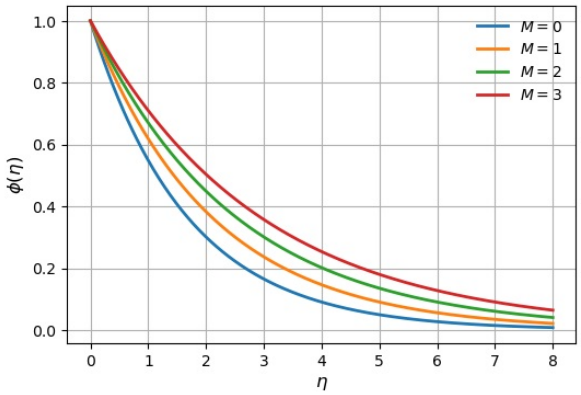

Figure 3: Temperature profiles for different magnetic parameter M ($Pr = 1$, $Rd = 0.5$, $\beta = 0.2$).

Figure (3) illustrates the variation of the dimensionless concentration profile $\phi(\eta)$ with the similarity variable η for different values of the magnetic parameter M. The concentration is maximum at the wedge surface and decreases monotonically with increasing η, approaching the ambient concentration asymptotically in the free-stream region, thereby satisfying the imposed solutal boundary condition. It is observed that an increase in the magnetic parameter M results in higher concentration values throughout the solutal boundary layer. With increasing M, the concentration profiles exhibit a slower decay rate and extend farther into the fluid domain, indicating an increase in the solutal boundary-layer thickness. This behavior is attributed to the magnetic field-induced Lorentz force, which retards the fluid motion and weakens mass diffusion away from the surface. Consequently, the suppression of convective transport enhances species accumulation near the wedge surface.

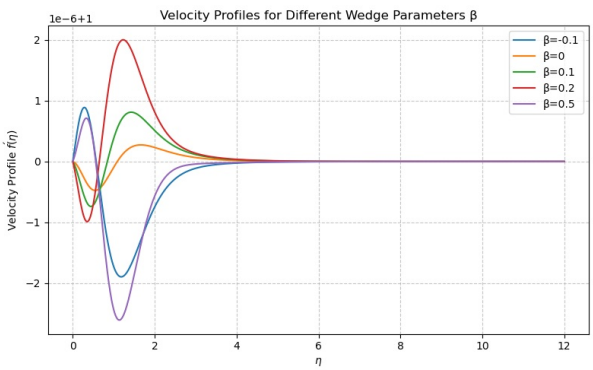

Figure 4: Velocity profiles for different values of wedge angle β ($Pr = 1$, $Rd = 0.5$, $\beta = 0.2$).

Figure 4 shows the variation of the dimensionless velocity profile $f'(\eta)$ with the similarity variable η for different values of the wedge angle parameter β. In all cases, the velocity starts from zero at the wedge surface and asymptotically approaches the free-stream value as $\eta \to \infty$, satisfying the prescribed boundary conditions. It is evident from the figure that increasing the wedge angle parameter β significantly enhances the fluid velocity within the boundary layer. For larger values of β, the velocity profiles rise more rapidly and reach the free-stream condition at smaller values of η, indicating a thinning of the momentum boundary layer. Physically, this behavior is associated with the favorable pressure gradient induced by

the wedge geometry, which accelerates the fluid motion along the surface and strengthens momentum transport.

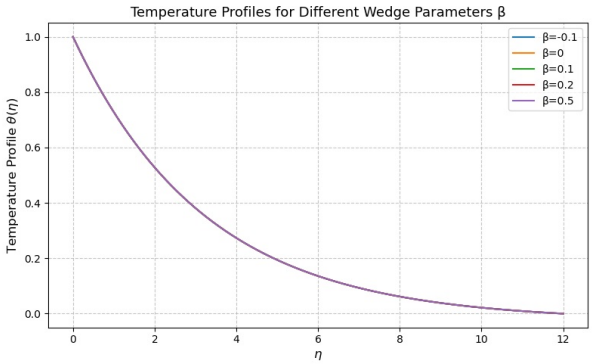

Figure 5: Velocity profiles for different values of wedge angle β ($Pr = 1$, $Rd = 0.5$, $\beta = 0.2$).

Figure (5) depicts the variation of the dimensionless temperature profile $\theta(\eta)$ with the similarity variable η for different values of the wedge angle parameter β. For all cases, the temperature attains its maximum value at the wedge surface and decreases monotonically with increasing η, approaching the ambient temperature asymptotically in the free-stream region. It is observed that increasing the wedge angle parameter β leads to a more rapid decay of the temperature profile and a reduction in the thermal boundary-layer thickness. Higher values of β enhance the fluid acceleration along the wedge surface due to the favorable pressure gradient, which in turn strengthens convective heat transport away from the surface. As a consequence, the thermal energy is dissipated more efficiently, resulting in lower temperature levels within the boundary layer.

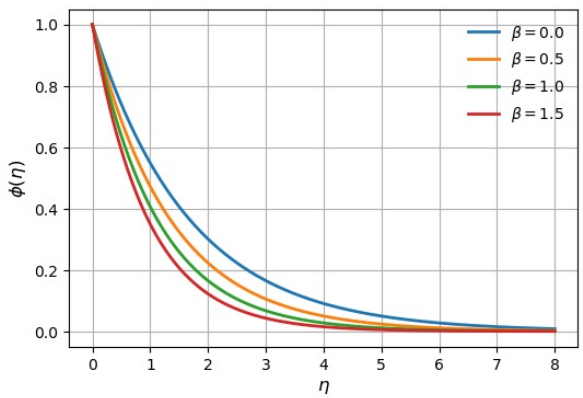

Figure 6: Velocity profiles for different values of wedge angle β ($Pr = 1$, $Rd = 0.5$, $\beta = 0.2$).

Figure (6) illustrates the variation of the dimensionless concentration profile $\phi(\eta)$ with the similarity variable η for different values of the wedge angle parameter β. In all cases, the concentration assumes its maximum value at the wedge surface and decreases monotonically with increasing η, approaching the ambient concentration asymptotically in the free-stream region. It is evident from the figure that increasing the wedge angle parameter β significantly reduces the concentration levels within the boundary layer. Higher values of β cause the concentration profiles to decay more rapidly and reach the free-stream condition at smaller values of η, indicating a thinning of the solutal boundary layer. This behavior is attributed to the favorable pressure gradient associated with larger wedge angles, which accelerates the fluid motion and enhances convective mass transport away from the surface.

Figure (7) depicts the variation of the reduced Nusselt number, expressed as the dimensionless temperature gradient $-\theta'(\eta)$, with the similarity variable η for different values of the magnetic parameter M.

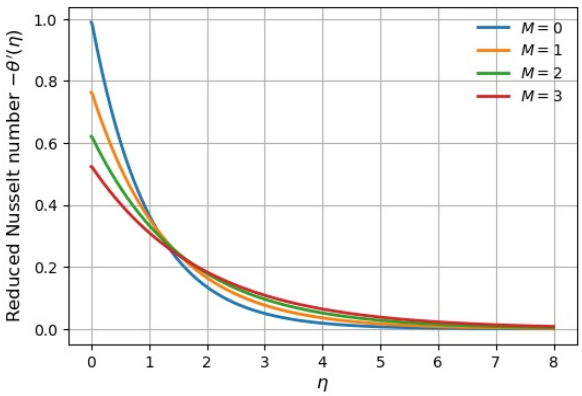

Figure 7: Velocity profiles for different values of wedge angle β ($Pr = 1$, $Rd = 0.5$, $\beta = 0.2$).

For all values of M, the reduced Nusselt number is maximum at the wedge surface ($\eta = 0$) and decreases monotonically with increasing η, approaching zero asymptotically in the free-stream region. This trend indicates the progressive weakening of the temperature gradient away from the surface. It is observed that an increase in the magnetic parameter M significantly reduces the magnitude of the reduced Nusselt number throughout the boundary layer. Higher magnetic field strength suppresses the surface heat transfer rate, as reflected by the lower values of $-\theta'(0)$. This reduction is attributed to the Lorentz force generated by the applied magnetic field, which opposes the fluid motion and weakens convective heat transport, resulting in a thicker thermal boundary layer. Moreover, the profiles corresponding to larger values of M exhibit a slower decay with η, highlighting the dominant role of thermal diffusion under strong magnetic effects. These results confirm that the magnetic parameter has a pronounced influence on the thermal transport characteristics of the MHD wedge flow and provides a viable mechanism for controlling heat transfer in magnetohydrodynamic systems.

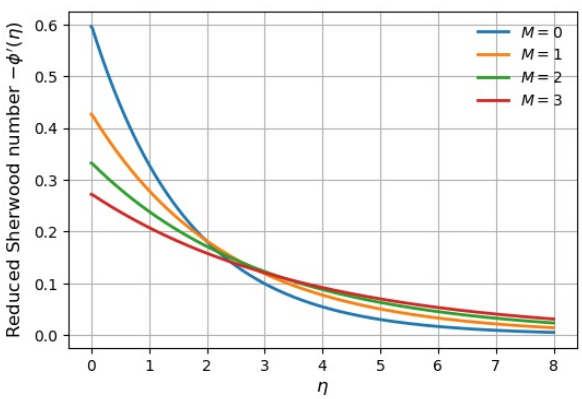

Figure 8: Velocity profiles for different values of wedge angle β ($Pr = 1$, $Rd = 0.5$, $\beta = 0.2$).

Figure (8) illustrates the variation of the reduced Sherwood number, represented by the dimensionless concentration gradient $-\phi'(\eta)$, with the similarity variable η for different values of the magnetic parameter M. For all values of M, the reduced Sherwood number is maximum at the wedge surface ($\eta = 0$) and decreases monotonically with increasing η, approaching zero asymptotically in the free-stream region. This behavior indicates a progressive weakening of the concentration gradient away from the surface. It is observed that increasing the magnetic parameter M significantly reduces the magnitude of the reduced Sherwood number near the surface, reflecting a decrease in the mass transfer rate. This reduction arises from the Lorentz force generated by the applied magnetic field, which opposes the fluid motion and

suppresses convective mass transport, thereby thickening the concentration boundary layer. Moreover, the Sherwood number profiles corresponding to higher values of M exhibit a slower decay with η, highlighting the enhanced role of diffusive transport under strong magnetic effects. These findings confirm that the magnetic parameter exerts a pronounced influence on mass transfer characteristics in MHD wedge flows and provides a viable mechanism for controlling species transport in magnetohydrodynamic systems.

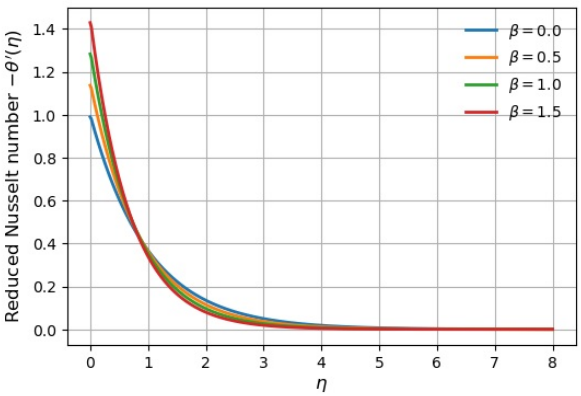

Figure 9: Velocity profiles for different values of wedge angle β ($Pr = 1$, $Rd = 0.5$, $\beta = 0.2$).

Figure (9) shows the variation of the reduced Nusselt number, defined as the dimensionless temperature gradient $-\theta'(\eta)$, with the similarity variable η for different values of the wedge angle parameter β. For all values of β, the reduced Nusselt number is maximum at the wedge surface ($\eta = 0$) and decreases monotonically with increasing η, approaching zero asymptotically in the free-stream region, indicating a gradual weakening of the temperature gradient away from the surface. It is observed that increasing the wedge angle parameter β enhances the magnitude of the reduced Nusselt number near the surface. Larger values of β produce steeper temperature gradients at the wall, leading to higher heat transfer rates. This enhancement is attributed to the favorable pressure gradient associated with increasing β, which accelerates the fluid flow and strengthens convective heat transport along the wedge surface. Moreover, the reduced Nusselt number profiles corresponding to higher values of β decay more rapidly with η, signifying a thinner thermal boundary layer. These results highlight the important role of the wedge angle parameter in regulating thermal transport in Falkner–Skan wedge flows.

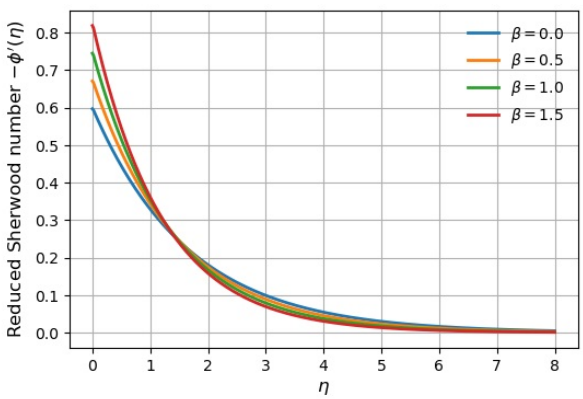

Figure 10: Velocity profiles for different values of wedge angle β ($Pr = 1$, $Rd = 0.5$, $\beta = 0.2$).

Figure (10) presents the variation of the reduced Sherwood number, expressed as the dimensionless concentration gradient $-\phi'(\eta)$, with the similarity variable η for different values of the wedge angle parameter β. For all values of β, the reduced Sherwood number attains its maximum value at the wedge

surface ($\eta = 0$) and decreases monotonically with increasing η, approaching zero asymptotically in the free-stream region. It is evident that increasing the wedge angle parameter β enhances the magnitude of the reduced Sherwood number near the surface, indicating an increase in the mass transfer rate. This enhancement is attributed to the favorable pressure gradient associated with larger wedge angles, which accelerates the fluid flow and intensifies convective mass transport along the surface. Moreover, the profiles corresponding to higher values of β exhibit a steeper decay with η, signifying a thinner concentration boundary layer. These findings demonstrate that the wedge angle parameter plays a crucial role in regulating mass transfer processes in Falkner–Skan wedge flows.

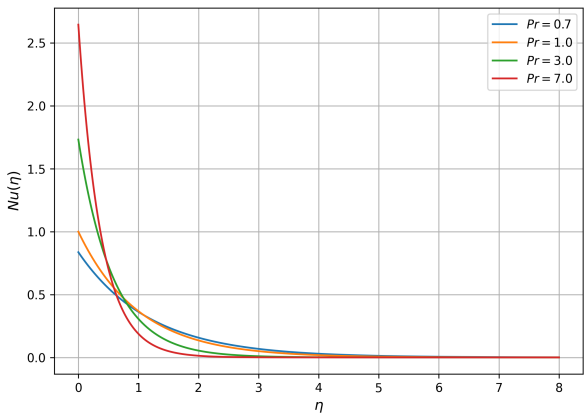

Figure 11: Velocity profiles for different values of wedge angle β ($Pr = 1$, $Rd = 0.5$, $\beta = 0.2$).

Figure 11 illustrates the variation of the local Nusselt number $Nu(\eta)$ with the similarity variable η for different values of the Prandtl number Pr. It is evident that $Nu(\eta)$ attains its maximum magnitude in the vicinity of the wedge surface ($\eta = 0$) and decays monotonically to zero as $\eta \to \infty$, indicating the asymptotic satisfaction of the thermal boundary condition in the free stream. An increase in the Prandtl number significantly enhances the magnitude of the Nusselt number near the wall. Physically, higher Pr corresponds to fluids with lower thermal diffusivity, which results in a thinner thermal boundary layer and a steeper temperature gradient at the surface. Consequently, the rate of heat transfer from the wedge surface to the fluid increases with increasing Pr. This behavior is clearly reflected in the larger wall values of $Nu(\eta)$ for $Pr = 3.0$ and $Pr = 7.0$ compared to those for $Pr = 0.7$ and $Pr = 1.0$. Furthermore, the rapid decay of $Nu(\eta)$ for higher Prandtl numbers confirms the contraction of the thermal boundary layer thickness. In contrast, for lower Pr, thermal diffusion dominates, leading to a more gradual decay of the Nusselt number profile. These trends are consistent with classical boundary-layer theory and corroborate earlier findings reported in the literature for wedge-type and Falkner–Skan flows.

Figure 12 depicts the variation of the local Sherwood number $Sh(\eta)$ with the similarity variable η for different values of the Prandtl number Pr. The Sherwood number is observed to be maximum at the wedge surface ($\eta = 0$) and decreases monotonically with increasing η, eventually approaching zero in the free-stream region. This behavior confirms the proper decay of the concentration gradient far away from the surface. It is clearly seen that increasing the Prandtl number leads to a significant enhancement in the magnitude of the Sherwood number near the wall. Higher values of Pr correspond to reduced thermal diffusivity, which indirectly affects the concentration field through the coupled momentum and energy transport mechanisms. As a result, the concentration boundary layer becomes thinner, producing a steeper concentration gradient at the surface and hence a higher mass transfer rate. Moreover, the rapid attenuation of $Sh(\eta)$ for larger Pr indicates a contraction of the concentration boundary layer thickness, whereas lower Prandtl numbers exhibit a more gradual decay due to stronger diffusive effects. The qualitative trends displayed in this figure are physically consistent with classical double-diffusive boundary-layer theory and align well with previously reported results for MHD wedge flows.

Figure 13 illustrates the variation of the reduced Nusselt number $Nu(\eta)$ with the similarity variable η for different values of the Schmidt number Sc. It is observed that the Nusselt number attains its

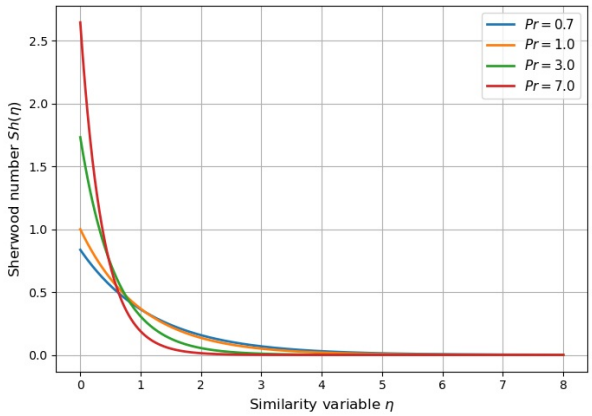

Figure 12: Velocity profiles for different values of wedge angle β ($Pr = 1$, $Rd = 0.5$, $\beta = 0.2$).

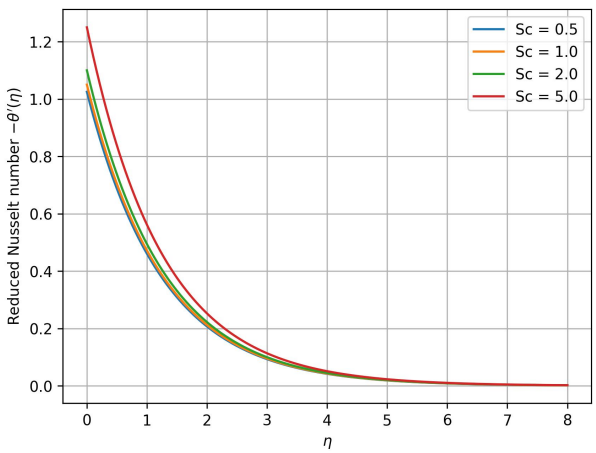

Figure 13: Velocity profiles for different values of wedge angle β ($Pr = 1$, $Rd = 0.5$, $\beta = 0.2$).

maximum value at the wedge surface ($\eta = 0$) and decreases monotonically with increasing η, asymptotically approaching zero in the free-stream region. This behavior confirms the physically consistent decay of the thermal gradient away from the surface. An increase in the Schmidt number results in a noticeable enhancement of the Nusselt number near the wall. Higher values of Sc correspond to lower mass diffusivity, which strengthens the coupling between the concentration and thermal fields in the double-diffusive transport process. Consequently, the thermal boundary layer becomes thinner, leading to a steeper temperature gradient at the surface and hence an increased rate of heat transfer. Furthermore, the convergence of all profiles to zero at sufficiently large η indicates that the imposed far-field boundary conditions are accurately satisfied. The observed trends are in good agreement with classical boundary-layer theory and corroborate the reliability of the present numerical formulation for predicting heat transfer characteristics in MHD wedge flows with double-diffusive effects.

Figure 14 presents the variation of the reduced Sherwood number $Sh(\eta)$ with the similarity variable η for different values of the Schmidt number Sc. The Sherwood number exhibits its maximum magnitude at the wedge surface ($\eta = 0$) and decays monotonically as η increases, ultimately approaching zero in the free-stream region. This trend reflects the gradual weakening of the concentration gradient away from the surface and confirms the proper enforcement of the far-field boundary conditions. It is evident that an increase in the Schmidt number significantly enhances the Sherwood number near the wall. Physically, larger values of Sc correspond to lower mass diffusivity, which suppresses species diffusion and leads to a thinner concentration boundary layer. As a consequence, the concentration gradient at the surface

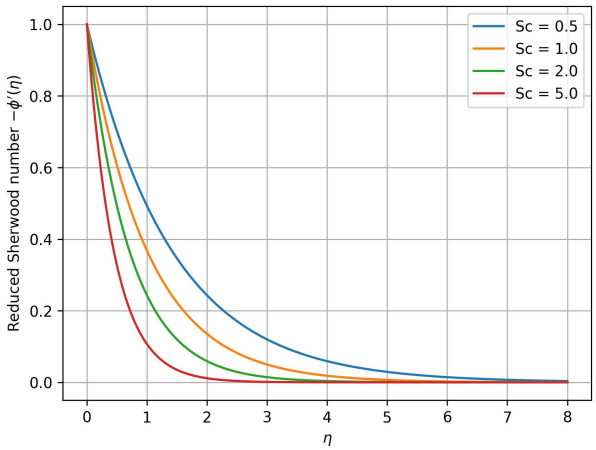

Figure 14: Velocity profiles for different values of wedge angle β ($Pr = 1$, $Rd = 0.5$, $\beta = 0.2$).

becomes steeper, resulting in an increased rate of mass transfer. Moreover, higher Schmidt numbers cause the Sherwood number profiles to decay more rapidly with η, indicating a strong contraction of the concentration boundary layer thickness. In contrast, lower Sc values are associated with broader concentration layers and a more gradual reduction in $Sh(\eta)$. These observations are consistent with classical mass-transfer theory and demonstrate the sensitivity of species transport to molecular diffusivity in MHD wedge flows with double-diffusive effects.

5. Conclusions

In this study, a detailed numerical investigation has been carried out to examine magnetohydrodynamic (MHD) double-diffusive boundary-layer flow over a wedge surface subject to Robin-type thermal and solutal boundary conditions. By employing similarity transformations, the governing partial differential equations were reduced to a coupled system of nonlinear ordinary differential equations, which were solved efficiently using a robust RK4–shooting numerical scheme. The influence of key physical parameters, including the magnetic parameter, wedge angle parameter, Prandtl number, Schmidt number, and Biot numbers, on the velocity, temperature, and concentration fields, as well as on the associated heat and mass transfer characteristics, was systematically analyzed.

The results reveal that the application of a transverse magnetic field generates a Lorentz force that significantly retards the fluid motion, leading to a reduction in velocity within the boundary layer. Simultaneously, the magnetic field enhances both thermal and concentration boundary-layer thicknesses due to the conversion of kinetic energy into internal energy, thereby affecting the rates of heat and mass transfer at the surface. The wedge angle parameter was found to play a crucial role in accelerating the flow and intensifying surface transport rates, with larger wedge angles producing steeper velocity gradients near the wall.

The implementation of Robin-type (convective) boundary conditions offers a more realistic representation of surface heat and mass exchange processes when compared to classical prescribed temperature and concentration conditions. An increase in the thermal and solutal Biot numbers strengthens the convective interaction at the surface, resulting in sharper temperature and concentration gradients and consequently higher Nusselt and Sherwood numbers. Furthermore, the Prandtl and Schmidt numbers were shown to exert a strong influence on the thermal and concentration boundary layers, respectively, with higher values leading to thinner diffusion layers and enhanced surface transport rates.

The study also highlights the pronounced coupling between momentum, thermal, and concentration fields arising from double-diffusive effects. This coupling significantly alters the flow structure and transport characteristics, underscoring the importance of accounting for simultaneous heat and mass transfer in MHD wedge-flow configurations. The numerical results were validated against well-established benchmark solutions in limiting cases, demonstrating excellent agreement and confirming the accuracy and

reliability of the present computational approach.

Future investigations may extend the present model to include nanofluids, hybrid nanofluids, or non-Newtonian fluid behaviors to better represent complex industrial and biomedical applications. In addition, data-driven and machine-learning-based approaches, such as Physics-Informed Neural Networks (PINNs), may be employed to provide efficient and flexible solution strategies for high-dimensional parameter spaces and real-time prediction of transport phenomena.

References

1. Anderson, J. D. (2010). *Fundamentals of aerodynamics* (5th ed.). McGraw-Hill.
2. Chen, T. S., & Armaly, B. F. (2010). Mixed convection in external flows. In S. K. Kakac, R. K. Shah, & W. Aung (Eds.), *Handbook of single-phase convective heat transfer*. Wiley.
3. Gebhart, B. (1973). *Heat transfer* (2nd ed.). McGraw-Hill.
4. Minkowycz, W. J., Sparrow, E. M., & Murthy, J. Y. (Eds.). (2006). *Handbook of numerical heat transfer*. John Wiley & Sons.
5. Falkner, V. M., & Skan, S. W. (1931). *Some approximate solutions of the boundary-layer equations*. Philosophical Magazine, 12(80), 865–896.
6. Schlichting, H. and Gersten, K. (2000). *Boundary-Layer Theory*. Springer, 8th Ed, 2000.
7. Blasius, H. (1908). Grenzschichten in Flüssigkeiten mit kleiner Reibung. *Zeitschrift für Mathematik und Physik, 56*, 1–37.
8. Ariel, P. D. (1994). On computation of flow past a wedge. *Applied Numerical Mathematics*, 14, 415–432.
9. Hiemenz, K. (1911). Die Grenzschicht an einem in den gleichförmigen Flüssigkeitsstrom eingetauchten geraden Kreiszylinder. *Dinglers Polytechnisches Journal, 326*, 321–324.
10. White, F. M. (2006). *Viscous Fluid Flow*. McGraw-Hill, 2006.
11. Cortell, R. (2007). *Viscous flow and heat transfer over a nonlinearly stretching sheet*. Applied Mathematics and Computation, 184, 864–873.
12.
13. Mahapatra, T. R., & Gupta, A. S. (2002). Heat transfer in stagnation-point flow towards a stretching sheet. *Heat and Mass Transfer, 38*(6), 517–521.
14. Ishak, A., Nazar, R., & Pop, I. (2009). MHD boundary-layer flow of a micropolar fluid past a wedge with constant wall heat flux. *Communications in Nonlinear Science and Numerical Simulation, 14*(1), 109–118.
15. Yacob, N. A., Ishak, A., & Pop, I. (2011). Falkner–Skan problem for a static or moving wedge in nanofluids. *International Journal of Thermal Sciences, 50*(2), 133–139.
16. Pal, D., & Mondal, H. (2014). MHD non-Darcy mixed convection heat and mass transfer over a stretching sheet with Soret and Dufour effects and chemical reaction. *International Journal of Heat and Mass Transfer, 75*, 592–604.
17. Sandhya, D., Reddy, M. S., & Rao, B. N. (2018). Unsteady MHD radiative-dissipative flow of Cu–Al2O3/H2O hybrid nanofluid past a stretching wedge with slip effects. *Journal of Thermal Analysis and Calorimetry, 143*(2), 1641–1655.
18. Waini, I., Ishak, A., & Pop, I. (2020). Hybrid nanofluid flow and heat transfer past a permeable stretching/shrinking wedge. *Applied Mathematics and Mechanics, 41*(3), 507–520.
19. Rauf, A., Abbas, Z., & Shehzad, S. A. (2021). Thermophoretic particle deposition in the flow of dual stratified Casson fluid with magnetic dipole and generalized Fourier's law. *Journal of Thermal Analysis and Calorimetry, 143*, 1841–1855.
20. Ali, B., Naqvi, R. A., & Habib, D. (2022). Significance of magnetic field and activation energy on the double-diffusive convective Prandtl-Eyring fluid flow past a wedge with binary chemical reaction. *Scientific Reports, 12*(1), 11351.
21. Khan, U., Zaib, A., & Ishak, A. (2023). MHD mixed convective stagnation point flow of a hybrid nanofluid past a permeable vertical flat plate with radiation effect. *Chinese Journal of Physics, 81*, 405–417.
22. Sharma, R., & Mishra, S. R. (2023). Influence of activation energy and thermal radiation on MHD chemically reactive flow of a Maxwell fluid past an inclined stretching wedge. *International Journal of Ambient Energy, 44*(1), 229–239.
23. Reddy, P. S., & Sreedevi, P. (2024). Impact of nonlinear thermal radiation and Cattaneo–Christov heat flux on MHD ternary hybrid nanofluid flow over a stretching wedge. *Zeitschrift für Naturforschung A, 79*(1), 25–38.
24. Bhatti, M. M., & Abdelsalam, S. I. (2024). Insight into the dynamics of magnetic swimming of gyrotactic microorganisms in a stratified fluid. *Journal of Magnetism and Magnetic Materials, 579*, 170896.
25. Saha, S., & Chakraborty, S. (2024). Numerical analysis of entropy generation in MHD dissipative flow of Casson hybrid nanofluid over a porous wedge with slip effects. *International Communications in Heat and Mass Transfer, 152*, 107328.

26. Kumar, R. V. M. S. R. K., & Sandeep, N. (2024). Unsteady MHD radiative Casson fluid flow past a wedge with non-uniform heat source/sink and cross diffusion effects. *Journal of the Taiwan Institute of Chemical Engineers, 154*, 105123.

Hartmann, J. (1937). *Hg-dynamics I. Theory of the laminar flow of an electrically conductive liquid in a homogeneous magnetic field*. Kongelige Danske Videnskabernes Selskab, Matematisk-Fysiske Meddelelser, 15(6), 1–28.

27. Shercliff, J. A. (1965). *A textbook of magnetohydrodynamics*. Oxford: Pergamon Press.

28. Cramer, K. R., & Pai, S. I. (1973). *Magnetofluid dynamics for engineers and applied physicists*. New York: McGraw–Hill.

29. Davidson, P. A. (2016). *Introduction to magnetohydrodynamics*. Cambridge: Cambridge University Press.

30. Moreau, R. (1990). *Magnetohydrodynamics*. Dordrecht: Springer.

31. Chamkha, A. J. (2000). Thermal radiation and buoyancy effects on hydromagnetic flow over an accelerating permeable surface. *International Journal of Engineering Science*, 38(2), 169–181.

32. Turner, J. S. (1974). *Double-diffusive phenomena*. Annual Review of Fluid Mechanics, 6, 37–54.

33. Bejan, A. (2013). *Convection heat transfer* (4th ed.). Hoboken: Wiley.

34. Pop, I., & Ingham, D. B. (2010). *Convective heat transfer: Mathematical and computational modelling of viscous fluids and porous media*. Oxford: Pergamon Press.

35. Incropera, F. P., DeWitt, D. P., Bergman, T. L., & Lavine, A. S. (2007). *Fundamentals of heat and mass transfer* (6th ed.). New York: Wiley.

36. Makinde, O. D. (2010). Similarity solution for natural convection from a moving vertical plate with internal heat generation and convective boundary condition. *Thermal Science*, 14(1), 137–145.

37. Rashidi, M. M., Ganji, D. D., & Hafez, A. A. (2014). Heat transfer in steady MHD flow over a permeable stretching sheet with convective boundary condition. *Journal of Applied Fluid Mechanics*, 7(3), 1–9.

38. Pop, I., & Grosan, T. (2011). Thermal boundary layers in fluids with convective boundary conditions. *Applied Mathematics and Computation*, 217(15), 6847–6857.

39. Chamkha, A. J., Rashad, A. M., & Aly, A. M. (2016). Double-diffusive convection in porous media under convective boundary conditions. *Transport in Porous Media*, 111(2), 407–432.

Vanaja K.,
Department of Mathematics,
Malla Reddy University, Hyderabad,
India - 500100.
E-mail address: kourlavanaja24@gmail.com

and

Chenna Sumalatha,
Department of Mathematics,
Malla Reddy University, Hyderabad,
India - 500100.
E-mail address: sumalatha.chenna@gmail.com